Journal of Crystal Growth 334 (2011) 146–152

Contents lists available at SciVerse ScienceDirect

Journal of Crystal Growth

journal homepage: www.elsevier.com/locate/jcrysgro

Three-dimensional phase-field crystal modeling of fcc and bcc dendritic crystal growth

Sai Tang [a,c], Rainer Backofen [b], Jincheng Wang [a], Yaohe Zhou [a], Axel Voigt [b], Yan-Mei Yu [c,*]

[a] State Key Laboratory of Solidification Processing, Northwestern Polytechnical University, Youyi Western Road 127, 710072 Xi'an, China
[b] Institut für Wissenschaftliches Rechnen, Technische Universität Dresden, 01062 Dresden, Germany
[c] Institute of Physics, Chinese Academy of Science, P. O. Box 603, 100190 Beijing, China

ARTICLE INFO

Article history:
Received 6 June 2011
Received in revised form
3 August 2011
Accepted 18 August 2011
Communicated by M. Plapp
Available online 26 August 2011

Keywords:
A1. Computer simulation
A1. Growth models
A1. Solidification
A1. Morphological stability

ABSTRACT

By using the phase-field crystal model (PFC), we simulate dendritic growth of face-centered cubic and body-centered cubic structures. The anisotropy of the dendritic growth velocity coefficient C and the growth dynamic scaling exponent n' are investigated as function of the PFC number density in the liquid phase $\overline{\psi}$. We obtain the stability criterion of the operating state of the PFC dendrite tip, which is about 0.278 (fcc) and 0.104 (bcc), being larger than 0.025 predicted for the macroscopic dendritic growth. This disagreement is caused by the strongly faceted growth in the regime of large anisotropy of the PFC surface energy.

1. Introduction

The dendritic growth is a long-standing fundamental research topic in materials science and materials processing. Its simulation is also a big challenge due to large time and space scales spanning atomic structures to macroscopic morphologies. At the atomic level, the molecular dynamics (MD) method has been used to evaluate various anisotropic properties of the solid–liquid interface that causes the dendritic growth [1–4]. However, long-time dendritic growth processes are not easily accessible in the MD simulations. At the macroscopic level, the coarsen-grained simulations like the phase-field (PF) method are instead adopted based on the input data of the anisotropy magnitude and the predefined formula of the crystal symmetry [5–9]. However, when the anisotropic strength is greater than 1/15, more complex regularization methods are required to amend the concavity in order to obtain the accurate crystal shape [10,11]. Recently, a new method known as phase-field-crystal (PFC) model [12–14] has been constructed based on the dynamical density-functional theory of freezing. Being implemented at the atomic length scale but the diffusive time scale, the PFC model can reproduce atomic processes of the anisotropic dendritic growth even without any input data of the anisotropy magnitude and the predefined formula of the crystal symmetry. Three-dimensional (3D) PFC phase diagrams have been proposed for the bcc phase [15] and also the fcc and hcp phases [16,17]. The previous study has shown that the single-component PFC model is possible to grow fcc and bcc dendrites [17]. The anisotropic growth properties has been done for flat interfaces of the fcc and bcc crystals in the PFC model, which is highly related to the dendritic growth [18]. Nevertheless, the anisotropic property of the dendritic growth still is not well-understood in the PFC simulations.

In this work, we reproduce the dendrite growth of the face-centered cubic (fcc) and bulk-centered cubic (bcc) structures by conducting large-scale PFC simulation in three dimensions. The anisotropic growth properties are further investigated by checking the growth velocity coefficient C and the growth dynamics n' for three low-index orientations [100], [110], and [111] (C and n' are obtained by fitting the position-time relationship $\delta Z = C\delta t^{n'}$, where δZ is variation of the growth front position in the time interval δt.) Our results show that $C_{[100]} > C_{[110]} > C_{[111]}$ (fcc) and $C_{[100]} > C_{[110]} \approx C_{[111]}$ (bcc), and for both fcc and bcc dendrites $n'_{[100]} = 1$ and $n'_{[110]} \approx n'_{[111]} < 1$. The anisotropy of C increases with the initial number density in the liquid phase $\overline{\psi}$, while the anisotropy of n' increases with the small parameter r (which controls anisotropy of the surface energy). Finally, we obtain the stability constant σ^* of the dendrite tip growth, which are $\sigma^* = 0.278$ (fcc) and $\sigma^* = 0.104$ (bcc). The faceting growth mechanism due to large PFC anisotropy is compared with the macroscopic dendritic growth of weak anisotropy.

* Corresponding author. Tel./fax: +86 10 82648059.
E-mail address: ymyu@aphy.iphy.ac.cn (Y.-M. Yu).

0022-0248/$ - see front matter © 2011 Elsevier B.V. All rights reserved.
doi:10.1016/j.jcrysgro.2011.08.027

2. Model

We first review derivation of the PFC model [13,15,19]. The PFC model is based on the classical density-functional theory (DFT) of freezing [20] that starts from a free-energy functional:

$$\frac{\Delta F[n(r)]}{k_B T\rho_0} = \int dr\{[1+n(r)]\ln[1+n(r)]-n(r)\} -\frac{1}{2}\int dr\int dr' n(r)\rho_0 c^{(2)}(|r-r'|)n(r'), \quad (1)$$

where $n(r)=[\rho(r)-\rho_0]/\rho_0$, $\rho(r)$ is the one-particle number density field, and ρ_0 is the one-particle number density of the reference liquid state. The local part is expanded as

$$[1+n(r)]\ln[1+n(r)]-n(r)\approx\frac{1}{2}n^2-\frac{a}{6}n^3+\frac{b}{12}n^4, \quad (2)$$

and the interaction function is expanded in the Fourier space as

$$C(k)=\rho_0\hat{C}(k)=C(k_m)-\Gamma\left(\frac{k_m^2-k^2}{k_m^2}\right)^2-E_B\left(\frac{k_m^2-k^2}{k_m^2}\right)^4, \quad (3)$$

where a, b, Γ, E_B are model parameters. The interaction function is related to the structure factor in terms of $S(k)=1/[1-C(k)]$. The PFC model parameters can be further determined in terms of k_m, $C''(k_m)$, C_0, and u_s, which are the position of the first maximum of $C(k)$, the second-order derivative of $C(k)$ at $k=k_m$, $C(k=0)$, and the amplitude of the density oscillation in the solid, respectively. The parameters in Eqs. (2) and (3) are expressed as

$$a=\frac{3}{2S(k_m)u_s}, \quad (4)$$

$$b=\frac{4}{30S(k_m)u_s^2}, \quad (5)$$

$$\Gamma=-\frac{k_m^2C''(k_m)}{8}, \quad (6)$$

$$E_B=C(k_m)-C_0-\Gamma. \quad (7)$$

By defining

$$n(r)=\overline{n}+\frac{\phi(r)}{\rho_0}, \quad (8)$$

Eq. (1) is rewritten as

$$F[\phi(r)]=\int dr\left\{\frac{1}{2}\phi(r)\left[\frac{k_BT}{\rho_0}(\omega(\nabla^2)-a\overline{n}+b\overline{n}^2)\right]\phi(r)+\frac{k_BTb}{12\rho_0^3}\phi^4(r)\right\}, \quad (9)$$

where $F[\phi(r)]=[\Delta F(\overline{n}+\phi(r)/\rho_0)-\Delta F(\overline{n})]/k_BT$, $\overline{n}=a/2b$ (by using this equality, the $\psi^3(r)$ term are removed), and

$$\omega(\nabla^2)=1-C(k_m)+\frac{\Gamma}{k_m^4}(k_m^2+\nabla^2)^2+\frac{E_B}{k_m^8}(k_m^2+\nabla^2)^4, \quad (10)$$

The governing evolution equation is then written as

$$\frac{\partial\phi}{\partial t'}=M_\rho\nabla^2\left(\frac{\delta F[\phi(r)]}{\delta\phi(r)}\right) =M_\rho\nabla^2\left\{\left[\frac{k_BT}{\rho_0}(\omega(\nabla^2)-a\overline{n}+b\overline{n}^2)\right]\phi(r)+\frac{k_BTb}{3\rho_0^3}\phi^3(r)\right\}. \quad (11)$$

Eq. (11) can be rewritten in the a Swift–Hohenberg-type form:

$$\frac{\partial\phi}{\partial t'}=M_\rho\nabla^2\{[\alpha+\lambda(k_m^2+\nabla^2)^2+\beta(k_m^2+\nabla^2)^4]\phi(r)+g\phi^3(r)\} \quad (12)$$

wherein

$$\alpha=\frac{k_BT}{\rho_0}\left(1-C(k_m)-\frac{a^2}{4b}\right) \quad (13)$$

$$\lambda=\frac{k_BT\Gamma}{\rho_0k_m^4}, \quad (14)$$

$$\beta=\frac{k_BTE_B}{\rho_0k_m^8}, \quad (15)$$

$$g=\frac{k_BTb}{3\rho_0^3}. \quad (16)$$

Introducing $x=k_m\vec{r}$, $t=\lambda k_m^6M_\rho t'$, and $\psi=\phi\sqrt{g/\lambda k_m^4}$, the dimensionless PFC model is written as

$$\frac{\partial\psi(x)}{\partial t}=\nabla^2\{[r+(1+\nabla^2)^2+\beta'(1+\nabla^2)^4]\psi(x)+\psi^3(x)\}, \quad (17)$$

where

$$r=\frac{\alpha}{\lambda k_m^4}=\left[1-C(k_m)-\frac{a^2}{4b}\right]/\Gamma, \quad (18)$$

$$\beta'=\frac{\beta}{\lambda}k_m^4=E_B/\Gamma, \quad (19)$$

where r is a small parameter. Substitute Eqs. (4)–(6) into Eq. (18), we can see that r is determined by properties u_s, k_m, $C(k_m)$, and $C''(k_m)$. Substitute Eqs. (6) and (7) into Eq. (19), we can see that β' is determined k_m, $C(k_m)$, $C''(k_m)$ and also C_0. Both r and β' depend on k_m (one of the important sources for the temperature dependence of these parameters). Furthermore, β' includes a new quantity C_0 to improve the approximation for the correlation function $C(k)$. The parameter β' arises from the eight-order fitting of $C(k)$ [19]. When $\beta'=0$, Eq. (17) reduces to the original PFC model [12,13] based on the fourth-order fitting of $C(k)$. In the previous study, Wu et al. have suggested $u_s=0.72$ and $r=0.0923$ for Fe (Table 1 of Ref. [15]), and Jaatinen et al. have suggested $1-C(k_m)=0.332$, $a=0.6917$, $b=0.0854$, $E_B=38.085$ and $\Gamma=11.583$ for Fe [19], which indicates $r=0.0923$, $\beta'=3.285$, and $\overline{\psi}=-0.2008$ (for $n_0=0$). The above data only suggests one point of the EOF PFC $(r,\overline{\psi})$ phase diagram, but most points in this $(r,\overline{\psi})$phase diagram are not available for EOF PFC model currently. Therefore, our following PFC computations shown

Table 1
The fitting results of the position–time relationship $Z=Z_0+C(t-t_0)^{n'}$ for various simulation parameters. The anisotropy of the growth velocity coefficient kinetics is defined by $\varepsilon^C=C_{[001]}/C_{[111]}$ (fcc) and $\varepsilon^C=C_{[001]}/C_{[110]}$ (bcc). The anisotropy of the growth dynamics index is defined by $\varepsilon_4^{n'}=(n_{[001]}-n'_{[110]})/(n_{[001]}+n'_{[110]})$. For C and n', the fitting error is less than 0.006 and 0.02 respectively. The small fitting error ensures that the best-fitting lines coincide with most data points of position–time plotted in Fig. 3.

Data set	Structure $(r,\overline{\psi})$	$C_{[100]}$	$C_{[110]}$	$C_{[111]}$	$n'_{[100]}$	$n'_{[110]}$	$n'_{[111]}$	ε^C	$\varepsilon_4^{n'}$
I	fcc(−0.53,−0.4607)	0.062	0.052	0.029	1.0	0.91	0.91	2.14	0.047
	fcc(−0.53,−0.4625)	0.058	0.040	0.026	1.0	0.925	0.92	2.23	0.039
	fcc(−0.53,−0.465)	0.045	0.034	0.023	1.0	0.92	0.92	1.96	0.042
	fcc(−0.53,−0.4675)	0.032	0.031	0.022	1.0	0.92	0.92	1.45	0.042
II	bcc(−0.30,−0.35)	0.070	0.052	0.054	1.0	0.94	0.96	1.35	0.03
	bcc(−0.25,−0.3205)	0.058	0.045	0.05	1.0	0.96	0.96	1.29	0.02
	bcc(−0.0923,−0.18)	0.22	0.22	0.22	1.0	1.0	1.0	1	0

in Section 3 are conducted for the case of $\beta' = 0$, i.e., based on the original PFC model. The parameters $(r,\overline{\psi})$ (as list in Table 1) are chosen based on the phase-diagram [16]. One of our PFC computations is for $r=-0.0923$ based on Wu's data [15] for Fe. However, it need to be note that our bcc dendrite obtained for $r=-0.0923$ is not the real iron dendrite, because such dendrite growth is a result of diffusive mass transport and the respective Mullins–Sekerka instability emerging from the over-damped conservative equation of motion of the PFC model, neither by the thermal field nor the solute field as the iron dendrite grows in real circumstances.

The one-mode approximations of the fcc and bcc structure are used as the initial input of ψ:

$$\psi_{fcc} = \overline{\psi} + 8A_s(\cos qx \cos qy \cos qz) \tag{20}$$

and

$$\psi_{bcc} = \overline{\psi} + 4A_s(\cos qx \cos qy + \cos qy \cos qz + \cos qz \cos qx), \tag{21}$$

where A_s and q are the amplitude and the wave number of the density fluctuation around an average density $\overline{\psi}$ respectively.

Eq. (17) is solved numerically using the semi-implicit Fourier spectral method with the space stepping $\Delta x = 1.0$ and the time stepping $\Delta t = 1.5$ on the simulation box of the size $L=800$ (fcc) and $L=1200$ (bcc). The dendrite growth begins with a sphere seed at center of the simulation box. In the center of the simulation domain a small spherical fcc or bcc nucleus is set according to Eqs. (20) and (21). The liquid around the initial nucleus is metastable due to the supersaturation of the liquid density. We develop a parallel C code using FFTW3 library, which is efficient for large-scale computations. The typical PFC computation for the bcc dendrite is conducted at $L=1200$ and $t=6000$ (the corresponding real space is about 3000 Å and the real time is about 10^{-6} s if taking the atomic lattice constant $a=3.3$ Å of the liquid metal and the self-diffusion coefficient of the liquid metal being $D=10^{-5}$ cm^2/s). The computations run on 50 CPU cores for 72 h on the supercomputer Mars at TU Dresden.

3. Results and discussion

The PFC dendrite morphology is shown in Fig. 1. For both fcc and bcc, six well-defined dendritic branches evolve in the $\langle 100 \rangle$ directions. The fcc dendrite in the [100] direction exhibits the four-fold symmetry. Away from the dendritic tip, the edges and faces of the dendritic branches change from the pyramidal structure towards a more parabolic shape gradually. The cross section parallel to the base of the fcc PFC dendrite still shows the four-fold symmetry of the dendrite tip. The dendritic faces consist of step trains. Towards the center of the grain the steps become denser and bent towards the dendrite tip. This effect, due to preferable kink production near the dendrite edges, may be the onset of a meandering instability at the dendrite faces. This leads to deep valleys in the dendrite faces or a fin structure as also reported for classical phase-field (PF) [7] and Kinetic-Monte-Carlo (KMC) [24] simulation of dendritic growth.

In Fig. 2(a) the locally smoothed density is shown. As predicted in the phase-diagram [16] the density in the crystal is higher than in the surrounding liquid. Ahead of the solid-liquid interface a depletion zone is formed in the liquid. Thus, the growth of the dendrite tip is driven by a Mullins–Sekerka type instability. The same mechanism can be accounted for the preferable kink production at the steps near the dendrite edges shown in Fig. 1. Fig. 2(b) illustrates the density distribution of ψ in three low-index growth directions. The [100] direction corresponds to the normal to the dendrite tip, the [011] direction corresponds to the normal to the interfaces in the saddle area between two dendrite branches, and the [111] direction corresponds to the

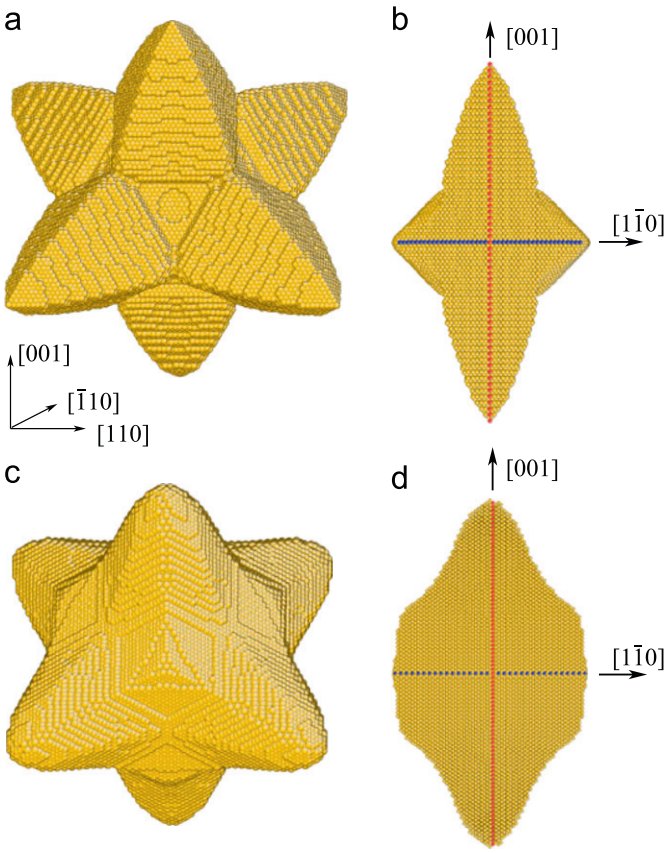

Fig. 1. The PFC dendrite morphology: (a) fcc $(r,\overline{\psi}) = (-0.53,-0.4607)$, containing about 77 039 atoms, (c) bcc $(r,\overline{\psi}) = (-0.30,-0.35)$, containing 250 000 atoms, and (b) and (d) show the corresponding cross-section images in the (110) plane.

normal to the interfaces in the valley area among three adjacent dendrite branches. The density ahead of the interfaces normal to [110] and [111] direction is remarkably lower than that ahead of the dendrite tip. We suppose that the more facile atomic attachment at steps and kinks on the surface normal to [011] and [111] direction is responsible for the lower density in the nearby area.

A closer analysis of the atomistic growth mechanism at the dendritic tip is shown in Fig. 2(c) and (d). Attaching of new layers leads to the fluctuating supersaturation at the dendrite tip. A fully facetted dendrite tip leads to the maximum of the supersaturation (D',D). After some time a new two dimensional island begins to nucleate at the {111} faces near the dendrite tip. As this island grows up, the local supersaturation reaches a minimum (A). When the island is fully formed, local supersaturation turns to increase again and the island begins laterally at the newly formed step edges and kinks (B,C). This leads to some smaller maximum of the local supersaturation at the interface again. Thus, the dendritic growth is defined by two dimensional nucleation at the {111} faces of the dendrite tip. The local supersaturation at the interface is connected to the amount of preferable attachment sites at the surface. The nucleation of the two dimensional island is the sources of the step trains that appear at the faces of the dendrite.

In order to analyze the anisotropic growth properties of the dendritic grain, we check the position-time relationship of the growth front for the principal directions [001], [110], and [111]. In Fig. 3, we fit the function of $Z = Z_0 + C(t-t_0)^{n'}$, where Z_0 and t_0 are position and time when the dendrite begins to evolve with constant velocity. The position–time relationship is also written as $V = Cn'(t-t_0)^{n'-1}$, wherein V is the dendritic growth velocity, n' is the dendritic dynamics exponent index, and C is the dendritic

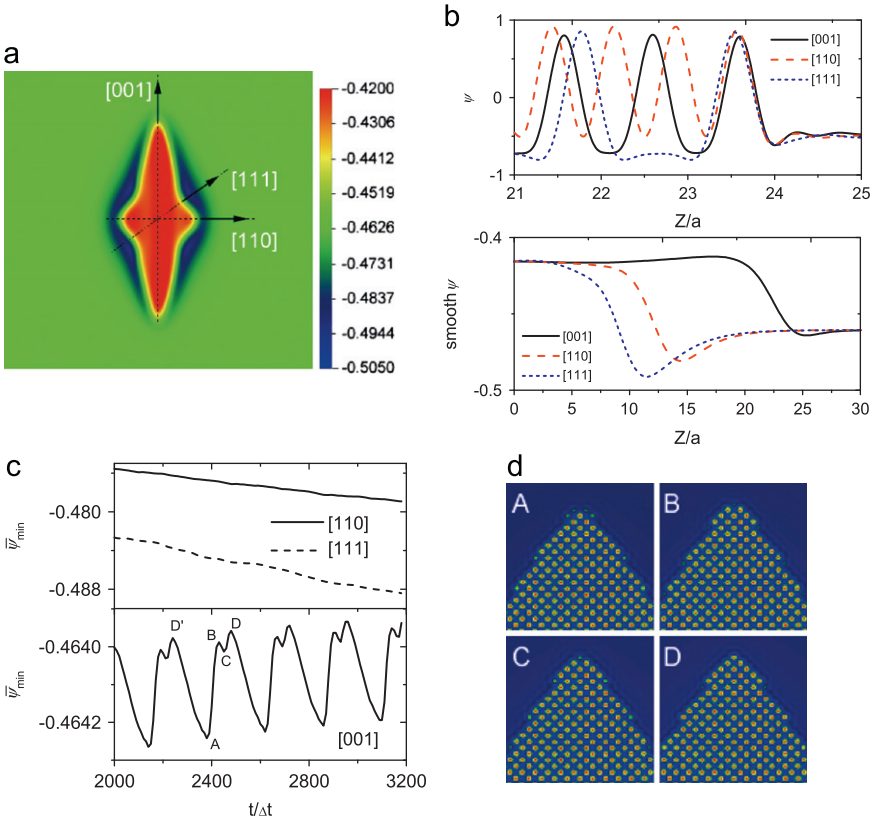

Fig. 2. The fcc dendritic growth simulated for $(r,\overline{\psi})=(-0.53,-0.4607)$: (a) the smooth density in the (110) cross-section plane, (b) the profile of the liquid density and its smooth value at the solid–liquid fronts, (c) variation of the minimum of the smooth density in the liquid front versus the time, (d) snapshots of the atomic structure of the dendrite tip at the time A, B, C, D, corresponding to half period of oscillation in the bellow panel in (c).

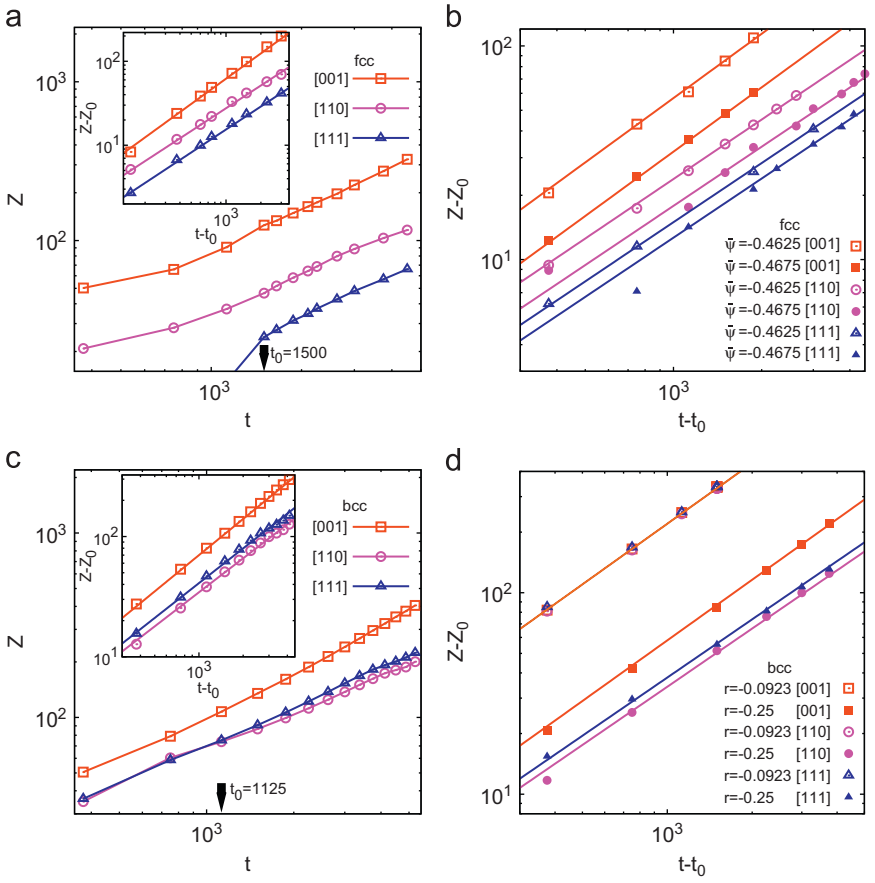

Fig. 3. The position Z of the dendritic growth front in [001], [110], and [111] orientations versus the growth time t plotted on the logarithmic coordination, where t_0 is the initial transient time for the steady state and Z_0 is the position at $t=t_0$. The function $Z=Z_0+C(t-t_0)^{n'}$ is fitted in the inset of (a) and (c). (a) fcc $(r,\overline{\psi})=(-0.53,-0.4607)$, (b) fcc $(r,\overline{\psi})=(-0.53,-0.4625)$ (open) and $(-0.53,\ -0.4675)$ (solid), (c) bcc $(r,\overline{\psi})=(-0.30,-0.35)$, and (d) bcc $(r,\overline{\psi})=(-0.0.0923,-0.18)$ (open) and $(-0.25,\ -0.3205)$ (solid). The fitting results are given in Table 1.

velocity coefficient. Table 1 gives our fitting results. We find that $n'=1$ in [001] directions for both fcc and bcc dendritic growth, whereas $n'<1$ in [110] and [111] directions ($n'_{[110]}\approx n'_{[111]}=0.91$ for the bcc dendritic growth and $n'_{[110]}\approx n'_{[111]}=0.96$ for the fcc dendritic growth). The scaling law $n'_{[001]}=1$ illustrates the constant-velocity growth, which is consistent with the dendritic growth experiment under the 'free' growth environment that has proven that the dendritic tip is of constant advancing velocity [25]. The scaling law $n'_{[110]}\approx n'_{[111]}<1$ further explain the anisotropic growth mechanism due to the Mullis–Sekeraka instability. We also find that $C_{[001]}>C_{[110]}>C_{[111]}$ (fcc) and $C_{[001]}>C_{[110]}\sim C_{[111]}$ (bcc). This result reflects that the crystal growth is facile in the [001] orientation, as supported by the geometric analysis of the fcc and bcc structure [26] and the MD results of the anisotropic atomic attachment kinetics, $\mu_{[001]}>\mu_{[110]}>\mu_{[111]}$ (fcc) and $\mu_{[001]}>\mu_{[110]}\sim\mu_{[111]}$ (bcc) [1,2,4]. Our results for C and n' illustrate the dendritic growth under the free growth mechanism, which is distinguished with the planar-interface crystal growth. For the latter the PFC simulation has predicted that $C_{[110]}>C_{[001]}$ and $C_{[111]}>C_{[001]}>C_{[110]}$ with $n'=0.5$ in terms of the diffusion-controlled growth mechanism [18].

The anisotropy of the dendrite growth is further investigated as a function of the PFC model parameters. The anisotropy of C is defined as $\varepsilon^C=C_{[001]}/C_{[111]}$ (fcc) and $\varepsilon^C=C_{[001]}/C_{[110]}$ (bcc). We find that ε^C increases with $\overline{\psi}$ (by comparing data of ε^C in Data set I in Table 1 for the same r value but different $\overline{\psi}$). This result seems to contradict to the trend observed for the flat interfaces of the bcc structure (in Ref. [18], Fig. 2(f) shows that the ratio of $C_{[100]}$ to $C_{[110]}$ seems to decrease with the increasing density). This contradiction is attributable to the fact that unlike that the flat interfaces are under diffusion-controlled growth mechanism, our dendritic growth is under 'free' growth mechanism. Where the energy can diffuse away rapidly, the dendritic growth is mainly determined by the local density. This tendency is most apparent in the [001] direction (where the local diffusion is most rapid). The larger liquid density causes the lager local growth velocity in [001] direction, which leads to that the reduced value of the corresponding ε^C increases versus the liquid density. The anisotropy of n' is defined as $\varepsilon_4^{n'}=(n_{[001]}-n'_{[110]})/(n_{[110]}+n'_{[110]})$. We find no obvious $\overline{\psi}$ dependence of $\varepsilon_{n'}^4$ (by comparing data of $\varepsilon_{n'}^4$ in Data set I in Table 1 for the same r value but different values of $\overline{\psi}$). On the other hand, we find that $\varepsilon_{n'}^4$ decreases with r through comparing $\varepsilon_{n'}^4$ for the different values of r (by comparing data of $\varepsilon_{n'}^4$ in Data set II in Table 1 for $r=-0.0923\sim-0.30$). Such results show that n' is affected mainly by r.

In our simulation, $n'=1$ is obtained for the dendritic tip, which indicates that the dendritic tip growth has entered into the stationary state, so that we can investigate the operating state of the dendrite tip in terms of the dendrite tip velocity $V_{\rm tip}$ and the dendrite tip radius R. The operating state of the dendrite tip is determinate by a stability criterion $\sigma^*=2Dd_0/R^2V_{\rm tip}$, where D is the diffusion constant in the liquid and d_0 is a capillary length defined by [5,21]

$$d_0=\begin{cases}\gamma/(\Delta c)^2(\partial\mu/\partial c) & \text{(chemical model)},\\ \gamma T_M C_P/L^2 & \text{(thermal model)},\end{cases}$$

where γ is the liquid–solid interface energy. In the chemical model, the dendritic growth is driven by the supersaturation of the chemical species, where Δc is the miscibility gap of the liquid–solid two phase region, μ is the chemical potential of the solute atoms relative to that of solvent, c is the concentration of the solute. In the thermal model, the dendritic growth is driven by the temperature undercooling, where T_M is the melt temperature of the pure substance, C_P is the specific heat capacity at constant pressure of the liquid, and L is the latent heat per unit volume of the solid. The dendrite growth in the PFC model is approximate to the chemical model, but driven by the density difference in liquid and solid in equilibrium, i.e., Δc .resp. $\Delta\phi$. Thus, in the PFC model, we can rewrite

$$\sigma^*=\frac{2\gamma M}{(\Delta\phi)^2V_{\rm tip}R^2}. \tag{22}$$

By using the dimension scales:

$$\gamma=\gamma'\lambda^2q_0^7/g, \tag{23}$$

$$\Delta\phi=\Delta\psi\sqrt{\lambda q^4/g}, \tag{24}$$

$$R=R'q_0^{-1}, \tag{25}$$

$$V=V'q_0^{-1}\lambda q_0^6M, \tag{26}$$

the dimensionless σ^* is rewritten as

$$\sigma^*=\frac{2\gamma'}{(\Delta\psi)^2V'_{\rm tip}R'^2} \tag{27}$$

In Fig. 4, we analyze the operate state of the dendrite tip of the fcc PFC dendrite obtained for $r=-0.53$ with the different $\overline{\psi}$. We extract the data for $V_{\rm tip}$ in terms of the position-time relationship of the dendrite tip. The tip radius is evaluated in the cross-section (110) plane that is cut along the principal [001] axis. The solid–liquid interface is defined by the position of the isoline of the smoothed density (that equals to the average value of the smooth liquid density and the smooth solid density). The positions of the solid-liquid interface is fitted in terms of $y=x^2/2R'+b$, where x and y are the x- and y-axis distance, R' is the dendrite tip radius, and b is a fitting parameter. For the facet dendritic morphology, R' is an effective size that reflects the sharpness of the dendrite tip as well as the average radian of the dendrite edges near the dendritic tip. The solid–liquid interface converges to a constant profile after the iterated filtering (e.g. the iteration time is taken to be 8–10 in our cases). Then, we can obtain the value of R' that is independent on the filtering. For high driving forces, that is increased by $\overline{\psi}$, $V'_{\rm tip}R'^2$ converges to a constant. The solid–liquid interfacial energy is calculated by constructing the Gibbs dividing surface for a crystal slab as proposed in [15,19]. We do two sets of calculations for σ^*, one for the fcc PFC dendrite obtained for $(r,\overline{\psi})=(-0.53,-0.4625)$, and the other for the bcc PFC dendrite obtained for $(-0.248,\ -0.323)$. The data for γ', $\Delta\psi$, V'_{tip} and R' are summarized in Table 2. We obtain $\sigma^*=0.278$ for the fcc PFC dendrite by adopting $\gamma'_{(111)}=0.0082$ and $\sigma^*=0.025\pm0.007$ for the bcc PFC dendrite by adopting $\gamma'_{(110)}=0.0027$. For the fcc $(-0.53,\ -0.4625)$ dendrite, the obtained value of R' evaluated in the (100)/(010) cross section plane (cut along the [001] principal, $R'=14.56$) is slightly larger than that evaluated in the

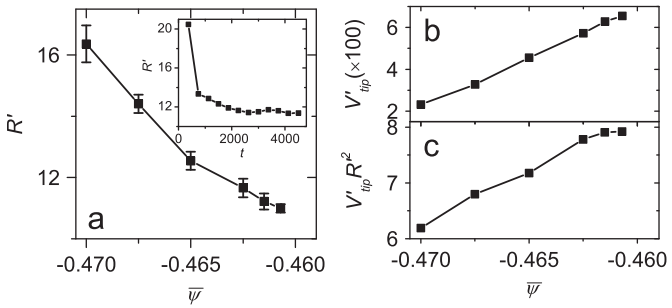

Fig. 4. The operate state for the dendrite tip obtained for $r=-0.53$ with the different $\overline{\psi}$. (a) The dendrite tip radius R', Inset: variation of R' versus time, reaching the steady state, obtained for $(r,\overline{\psi})=(-0.53,-0.4625)$. Oscillation of R' at the steady state is denoted by the error bar. (b) The dendrite tip growth velocity $V'_{\rm tip}$. (c) $V'_{\rm tip}R'^2$.

Table 2
Results of the PFC simulations for the interface energy γ' and its anisotropy ε_4, the dendritic tip velocity V'_{tip}, the dendritic tip radius R', and the reduced stability constant σ^*. The error bar for σ^* comes from fluctuation of R' versus time, and $\varepsilon_4=(\gamma_{[001]}-\gamma_{[111]})/(\gamma_{[001]}+\gamma_{[111]})$ (fcc) and $\varepsilon_4=(\gamma_{[001]}-\gamma_{[110]})/(\gamma_{[001]}+\gamma_{[110]})$ (bcc).

Structure$(r,\overline{\psi})$	$\gamma'_{(100)}$	$\gamma'_{(110)}$	$\gamma'_{(111)}$	ε_4	$\Delta\psi$	V'_{tip}	R'	σ^*
fcc$(-0.53,-0.4625)$	0.0113	–	0.0082	0.16	0.087	0.057	11.66	0.278 ± 0.017
bcc$(-0.248,-0.323)$	0.0031	0.0027	–	0.074	0.034	0.049	30.39	0.104 ± 0.006

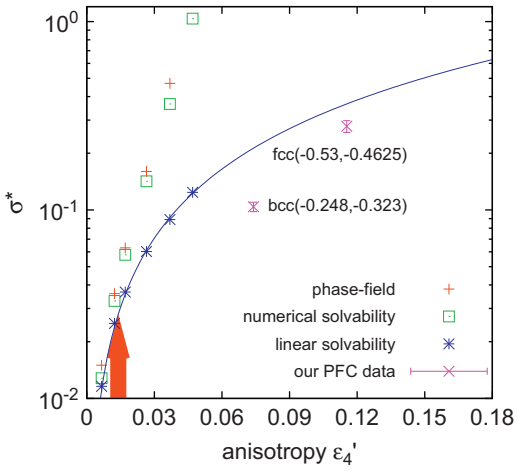

Fig. 5. The stability constant σ^* versus the crystal anisotropy ε'_4 compared with the reported data in Ref. [5]. The red arrow denotes $\sigma^*=0.025\pm0.007$ for weak anisotropy of ε'_4 generally cited in Refs. [7,21–23]. (For interpretation of the references to color in this figure legend, the reader is referred to the web version of this article.)

(110) cross section plane ($R'=12.66$). Larger R' indicates lower σ^* (σ^* is proportional to $1/R'^2$). For bcc $(-0.248,\ -0.323)$, R' evaluated in the (110) plane and that evaluated in the (100)/(010) plane are the same.

Our results of σ^* are larger than the predicted value that generally cited for the macroscopic dendritic growth in an ingot of molten metal or SCN [21–23]. The phase-field simulation also predicted σ^* being about 0.025 in the regime of ε_4 being around 0.01–0.02 [5–7]. Our PFC simulations are conducted for large values of ε_4 ($\varepsilon_4=0.16$ for fcc $(-0.53,\ -0.4625)$ and $\varepsilon_4=0.074$ for bcc $(-0.248,\ -0.323)$. For such ε_4 values, the growth mechanism is governed by two dimensional nucleation near the dendrite tip and step flow along the dendrite faces, which corresponds to the slower growth velocity and the sharper tip radius. Therefore, our results of σ^* locate on the large side, corresponding to the high ε_4 values. Fig. 5 compares our data of σ^* with the reported data in Ref. [5] for the different ε_4. Here, ε_4 is related to ε'_4 (the anisotropy coefficient defined in Ref. [5]) in terms of $\varepsilon_4=4\varepsilon'_4/(3-\varepsilon'_4)$. Our results are close to the data obtained by the Liner stability theory. However, we give the PFC results for only two points of anisotropy, which still is insufficient to make a complete comparison with the previous theories. Besides, its need to be note that Fig. 5 only is a qualitative comparison. So far, there is no effective way to convert the PFC model parameter $(r,\overline{\psi})$to the temperature undercooling or the solute supersaturation that are used in real cases. Here, we define an effective supersaturation as $(\overline{\psi}-\overline{\psi}_{liquidus})/(\overline{\psi}_{solidus}-\overline{\psi}_{liquidus})$, where $\overline{\psi}_{solidus}/\overline{\psi}_{liquidus}$ is the density at the solidus/liquids line. In our cases the effective supersaturation equals to 0.96 and 0.87 for fcc $(-0.53,\ -0.4625)$ and bcc $(-0.248,\ -0.323)$ respectively, which means that there is very large density supersaturation in the initial liquid. However, our PFC supersaturation is not equivalent to the solute supersaturation in real cases. Therefore, the above comparison of our PFC and the previous theories is qualitative on the precondition that the corresponding undercooling/superdaturation used in our PFC simulations may be different from those used in the previous theories. To conduct the PFC simulation for dendritic growth especially for weak ε_4 is still a challenging task, which requires larger simulation system size. In real dendritic growth, the MS instability is driven by solute or thermal diffusion. The binary PFC modeling works have been done in this field [14,27]. To conduct PFC simulation for real dendrites brings a big challenge for the ongoing research.

4. Conclusions

We investigated the fcc and bcc PFC dendritic growth for large ε_4. Our results reproduce the anisotropic growth process of the fcc and bcc PFC dendrites at the atomic level. The growth mechanism is described by two dimensional nucleation near the dendrite tip serving as a source for step flow at faces of the dendrite. The growth velocity coefficient C and the growth dynamics n' are checked for three low-index orientations [100], [110], and [111]. Our results show $C_{[100]}>C_{[110]}>C_{[111]}$ (fcc) and $C_{[100]}>C_{[110]}\approx C_{[111]}$ (bcc), and $n'_{[100]}=1$ and $n'_{[110]}\approx n'_{[111]}<1$ for both fcc and bcc dendrites. The anisotropy of C increases with $\overline{\psi}$ while the anisotropy of n' increases with r. In the regime of large PFC anisotropy, the faceted growth of the PFC dendrite forms the sharp dendritic tip, which leads to large σ^*, about 0.278 (fcc) and 0.104 (bcc), deviating from $\sigma^*=0.025$ predicted for the macroscopic dendritic growth of weak anisotropy of the crystal structure.

Acknowledgements

This work has been supported by Nature Science Foundation of China (Grant Nos. 10974228, 51071128), and the fund of the State Key Laboratory of Solidification Processing in NWPU (SKLSP201001), Program for New Century Excellent Talents in University, and the Doctorate Foundation of Northwestern Polytechnical University(CX201106). We further acknowledge support by DFG through Vo 899/7 and the computing resources at TU Dresden.

References

[1] J.J. Hoyta, M. Asta, A. Karma, Materials Science and Engineering R 41 (2003) 121.
[2] D.Y. Sun, M. Asta, J.J. Hoyta, Physics Review B 69 (2004) 174103.
[3] M. Amini, B.B. Laird, Physics Review L 97 (2006) 216102.
[4] Z.G. Xia, D.Y. Sun, M. Asta, J.J. Hoyt, Physics Review B 75 (2007) 012103.
[5] A. Karma, W.J. Rappel, Physics Review Letters 77 (1996) 4050.
[6] A. Karma, W.J. Rappel, Physics Review E 57 (1998) 4323.
[7] A. Karma, Y.H. Lee, M. Plapp, Physics Review E 61 (2000) 03996.
[8] T. Haxhimali, A. Karma, F. Gonzales, M. Rappaz, Nature Materials 5 (2006) 660.
[9] J. Warren, Nature Materials 5 (2006) 595.
[10] J.J. Eggleston, G.B. McFadden, P.W. Voorhees, Physics D 150 (2001) 91.
[11] H.K. Lin, C.C. Chen, C.W. Lan, Journal of Crystal Growth 318 (2011) 51.
[12] K.R. Elder, M. Katakowski, M. Haataja, M. Grant, Physics Review Letters 88 (2002) 245701.
[13] K.R. Elder, M. Grant, Physics Review E 70 (2004) 051605.
[14] K.R. Elder, N. Provatas, J. Berry, P. Stefanovic, M. Grant, Physics Review B 75 (2007) 064107.
[15] K.A. Wu, A. Karma, Physics Review B 76 (2007) 184107.

[16] A. Jaatinen, T. Ala-Nissila, Journal of Physics: Condensed Matters 22 (2010) 205402.
[17] G.I. Toth, G. Tegze, T. Pusztai, G. Toth, L. Granasy, Journal of Physics: Condensed Matters 22 (2010) 364101.
[18] G. Tegze, L. Gránásy, G.I. Tóth, F. Podmaniczky, A. Jaatinen, T. Ala-Nissila, T. Pusztai, Physics Review Letters 103 (2009) 035702.
[19] A. Jaatinen, C.V. Achim, K.R. Elder, T. Ala-Nissila, Physics Review E 80 (2009) 031602.
[20] T.V. Ramakrishman, M. Yussouff, Physics Review B 19 (1979) 2775.
[21] J.S. Langer, Reviews of Modern Physics 52 (1980) 1.
[22] A. Barbieri, J.S. Langer, Physics Review A 39 (1989) 5314.
[23] J.C. LaCombe, M.B. Koss, J.E. Frei, C. Giummarra, A.O. Lupulescu, M.E. Glicksman, Physics Review E 65 (2002) 031604.
[24] T. Schulze, Physics Review E 78 (2008) 020601.
[25] S.C. Huang, M.E. Glicksman, Acta Metallurgica 29 (1981) 701.
[26] C. Chattopadhyay, S. Sangal, K. Mondal, Acta Metallurgica 58 (2010) 5342.
[27] N. Provatas, J.A. Dantzig, B. Athreya, P. Chan, P. Stefanovic, N. Goldenfeld, K.R. Elder, Journal of Materials 59 (2007) 87.